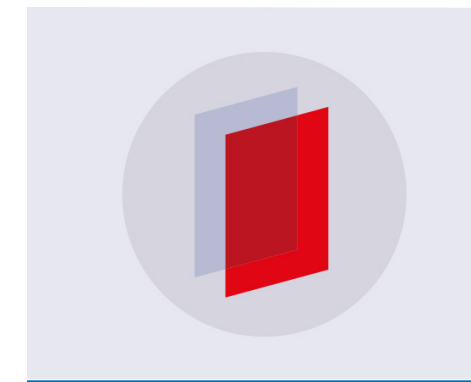
#### **PAPER**

## Approximation of continuous EIT data from electrode measurements with Bayesian methods

To cite this article: D Calvetti et al 2019 Inverse Problems 35 045012

View the <u>article online</u> for updates and enhancements.



### IOP ebooks™

Bringing you innovative digital publishing with leading voices to create your essential collection of books in STEM research.

Start exploring the collection - download the first chapter of every title for free.

# Approximation of continuous EIT data from electrode measurements with Bayesian methods

#### D Calvetti<sup>®</sup>, S Nakkireddy and E Somersalo<sup>®</sup>

Department of Mathematics, Applied Mathematics and Statistics, Case Western Reserve University, 10900 Euclid Avenue, Cleveland, OH 44106, United States of America

E-mail: erkki.somersalo@case.edu

Received 23 September 2018, revised 10 January 2019 Accepted for publication 12 February 2019 Published 27 March 2019



#### **Abstract**

The electrical impedance tomography (EIT) in its classical formulation seeks to estimate the electric conductivity distribution inside the body from the knowledge of the Dirichlet-to-Neumann (DtN) map of the conductivity equation at the boundary. Numerical methods for the solution of the EIT problem have been developed based on this formulation, most notably the d-bar method and the layer stripping algorithm. In practice, however, the EIT data (electrode data), collected by using a fixed number of contact electrodes, is tantamount to knowledge of the resistance matrix, a mapping between given current configuration and the corresponding vector of measured electrode voltages. Forward models corresponding to the DtN data and the electrode data differ in terms of the boundary values and no direct connection between them has been established. In this article, we analyze the relation between the two boundary data types, and propose to approximate the DtN data from the measured resistance matrix for solving the EIT inverse problem within the Bayesian framework, leveraging a sample based prior and a principal component model reduction.

Keywords: Dirichlet-to-Neumann, principal component analysis, complete electrode model

(Some figures may appear in colour only in the online journal)

#### 1. Introduction

The goal of electrical impedance tomography (EIT) is to estimate the electrical conductivity distribution inside a body from current/voltage measurements at the boundary. Two different, but mathematically equivalent boundary measurements can be used as input for the EIT problem. The first consists of the measurements of the current density on the boundary caused by a voltage distribution applied on it, while in the second a current distribution is applied on the boundary and the resulting voltage is measured. In mathematical terms, the first protocol correspond to determining the Dirichlet-to-Neumann (DtN) map of the elliptic differential operator describing the voltage distribution, while the second is tantamount to determining the Neumann-to-Dirichlet (NtD) map of the operator. The tradition of choosing the Dirichlet-to-Neumann map as the starting point for the mathematical analysis of the EIT inverse problem can be traced to the seminal paper of Calderón [2]. The analysis based on the complex geometrical optics (CGO) solutions of the conductivity equation not only answered successfully to the question of unique solvability of the mathematically idealized EIT inverse problem, or the Calderón problem [21, 29], but also set the foundations for a computational approach to the numerical estimate of the conductivity from idealized boundary data [20, 26]. A different approach relying on the idealized boundary data is the layer stripping algorithm [27], which artificially propagates the boundary operator, either DtN or NtD, concomitantly estimating the conductivity inside of the body along layers which are progressively peeled off as in an onion as the propagation proceeds. For other analytical approaches relying on continuous boundary data, we mention the factorization method [19], the enclosure method [15], and the monotonicity method [10, 30].

In practice, the idealized continuous boundary data are not directly available, as realistic EIT data are collected by attaching a number of contact electrodes on the surface of the body, and injecting known currents through the electrodes while measuring the voltages, or alternatively applying known voltage potentials on electrodes, and measuring the current densities through them. The former protocol, known as applied current tomograph is a discrete counterpart of the Neumann-to-Dirichlet map [7], while the latter, referred to as applied potential tomograph, providies a discrete version of the Dirichlet-to-Neumann data [1]. These methods lead to either a resistance matrix or a conductance matrix, which do not directly approximate accurately the respective continuous boundary maps because the conducting electrodes create a shunt effect along the boundary that needs to be taken into account, and current densities and voltage distributions cannot be controlled with resolution beyond the electrode size. A practical approach to overcome these limitations is to approximate the current densities by assuming a constant current density through each electrode, known as the 'gap model', and estimate the continuous mapping in the Fourier basis corresponding to this approximation [16, 17].

Another alternative, which we investigate in this paper, is to carefully account for the electrodes by means of the complete electrode model (CEM) [8, 28], and use the detailed model to estimate the continuous boundary operator from the data.

The approximation of the continuous data based on the electrode data has been addressed in the literature [13, 14], by using appropriate non-orthogonal projections, and convergence in the limit as the number of electrodes goes to infinity is proved. In [12], the authors considered data collected with point-like electrodes, that would reduce the effect of the electrodes, and in particular the contact impedance, on the data.

In this paper, using the variational forms of the forward models, we derive an analytic formula coupling the resistance matrix of the electrode data and the infinite dimensional matrix of the Dirichlet-to-Neumann map in terms of the Fourier basis. The problem of estimating the continuous map from this relation is ill-posed, and we propose to solve the problem by means

of a Bayesian statistical model reduction technique that augments the measured electrode data with prior information about the boundary map. The viability of the proposed approach and its computational efficiency are demonstrated by computed numerical examples. An outline of the results is given below.

Consider a bounded domain  $\Omega$  with connected boundary, and a conductivity  $\sigma > 0$  defined in it. The electric voltage potential with prescribed Dirichlet boundary values satisfies

$$\nabla \cdot (\sigma \nabla u) = 0 \text{ in } \Omega, \tag{1}$$

$$u\big|_{\partial\Omega} = f. \tag{2}$$

The Dirichlet-to-Neumann map for this problem is defined as

$$\Lambda_{\sigma}: f \mapsto \sigma \frac{\partial u}{\partial n} \bigg|_{\partial \Omega},$$

the exact regularity assumptions being described later in the discussion. The classical Calderón problem is to reconstruct the conductivity  $\sigma$  from the knowledge of  $\Lambda_{\sigma}$ . Assume that a finite number of electrodes  $e_{\ell} \subset \partial \Omega$ ,  $1 \leq \ell \leq L$ , are attached to the boundary of the body. Given electric currents  $J_{\ell}$  are injected through each electrode, thus generating a voltage potential v that satisfies the equation (1) in  $\Omega$ , and a voltage  $V_{\ell}$  at each electrode  $e_{\ell}$ . Each electrode has its characteristic contact impedance  $z_{\ell} > 0$ , and according to the complete electrode model (CEM), the voltage potential and electrode voltages satisfy the boundary conditions

$$\int_{e_{\ell}} \sigma \frac{\partial v}{\partial n} dS = J_{\ell}, \quad 1 \leqslant \ell \leqslant L, \tag{3}$$

$$\sigma \frac{\partial v}{\partial n} \Big|_{\partial \Omega \setminus \cup_{\ell=1}^{L} e_{\ell}} = 0, \tag{4}$$

$$\left(v + z_{\ell} \, \sigma \frac{\partial v}{\partial n}\right) \bigg|_{e_{\ell}} = V_{\ell}, \quad 1 \leqslant \ell \leqslant L. \tag{5}$$

Equation (3) gives the total current through the electrode, (4) expresses the condition that there is no current flow between electrodes, and, finally, (5) relates the electrode voltages to the interior voltage potential: if  $z_{\ell} = 0$  the condition simply states that the electrode is a perfectly conducting shunt. Finally, the conservation of current requires that Kirchhoff's law is satisfied:

$$\sum_{\ell=1}^{L} J_{\ell} = 0. {(6)}$$

The resistance matrix is defined as  $R_{\sigma} \in \mathbb{R}^{L \times L}$ , such that

$$R_{\sigma}J=V$$
.

The EIT problem with the complete electrode model is to estimate  $\sigma$  from the knowledge of  $R_{\sigma}$ . The basic problem addressed here is, how to approximate  $\Lambda_{\sigma}$  if  $R_{\sigma}$  is measured.

In section 2, by using the variational formulations of the continuous model and the electrode model, we derive an integral equation that connects the two operators. This connection, which is the main result of that section, is established in theorem 2.2.

In actual computations, the Dirichlet-to-Neumann map needs to be approximated by a finite matrix. Limiting the discussion here to two dimensions, we represent the operator in Fourier basis, and establish the matrix formula that connects  $R_{\sigma}$  with the infinite matrix representation of  $\Lambda_{\sigma}$  in theorem 3.3. This formula shows the anticipated result that recovering the matrix  $R_{\sigma}$  from the knowledge of  $R_{\sigma}$  is a straightforward well-posed problem, while the converse is not.

The estimation of the Dirichlet-to-Neumann matrix is an ill-posed problem, and to approach it computationally, we recast it in the Bayesian setting. Since there is no immediate way to define a feasible prior model for  $\Lambda_{\sigma}$  directly, we suggest an indirect approach: we define a prior model for the conductivities in  $\Omega$ , and by sampling from the prior, we compute a sample of the corresponding Dirichlet-to-Neumann maps using the finite element method. In line with standard principal component analysis (PCA) model reduction techniques, we represent the Dirichlet-to-Neumann maps as linear combinations of a limited number of principal feature vectors, thus reducing the estimation problem to a least squares problem of low dimensionality, defined in problem 4.1.

The computational details concerning the finite element approximations and sampling are presented in section 5, where we also show that both the Dirichlet-to-Neumann matrix and the resistance matrix can be written as Schur complements of appropriate partitionings of the stiffness matrix of the respective boundary value problem. Finally, the feasibility of the approach is tested by few computed examples in section 6.

#### 2. Complete electrode model and continuous boundary data model

In this section we review the continuous boundary data model and the discrete electrode model, establishing the connection between them through the variational formulations that constitute the basis for our computational approach.

Let  $\Omega \subset \mathbb{R}^n$ , n=2,3, be a bounded domain with connected boundary  $\partial\Omega$  representing the body of interest, and let  $\sigma \in L^\infty(\Omega)$  denote the conductivity distribution in  $\Omega$ . In practice, however, since the discretization of the variational forms is limited to conductivities represented in a mesh basis, we assume that  $\sigma$  is a piecewise smooth function, with constants  $0 < \sigma_m \leqslant \sigma_M < \infty$  such that

$$\sigma_m \leqslant \sigma(x) \leqslant \sigma_M, \quad x \in \Omega,$$

and that the voltage potential u in  $\Omega$  satisfies the continuity equation (1). Below, we review briefly some of the basic properties of the solutions with different boundary conditions.

Continuous boundary data: Consider the equation (1) with the Dirichlet boundary condition

$$u\big|_{\partial\Omega} = f \in H^{1/2}(\partial\Omega). \tag{7}$$

The standard variational formulation of the Dirichlet problem is obtained by multiplying the equation (1) by a test function  $w \in H^1(\Omega)$ ; after an integration by parts, using the boundary condition (7), we arrive at the identity

$$\int_{\Omega} \sigma \nabla w \cdot \nabla u dx = \int_{\partial \Omega} w \sigma \frac{\partial u}{\partial n} dS = \langle w, \Lambda_{\sigma} f \rangle, \tag{8}$$

where  $\Lambda_{\sigma}$  is the Dirichlet-to-Neumann map:

$$\Lambda_{\sigma}: H^{1/2}(\partial\Omega) \to H^{-1/2}(\partial\Omega), \quad u\big|_{\partial\Omega} \mapsto \sigma \frac{\partial u}{\partial n}\bigg|_{\partial\Omega},$$

and  $\langle \cdot, \cdot \rangle$  denotes the duality between the Sobolev spaces  $H^{1/2}(\partial\Omega)$  and  $H^{-1/2}(\partial\Omega)$  extending the integral over the boundary.

The following theorem states some basic properties of the Dirichlet-to-Neumann map that will be needed later.

**Theorem 2.1.** The Dirichlet-to-Neumann map is self-adjoint and positive, with the null space and range

$$\mathcal{N}(\Lambda_{\sigma}) = \text{span}\{1\}, \quad \mathcal{R}(\Lambda_{\sigma}) = \text{span}\{1\}^{\perp}.$$

This well-known result is based on the observation that if  $u^f$ ,  $u^g \in H^1(\Omega)$  are solutions of the equation (1) with Dirichlet data,  $f, g \in H^{1/2}(\partial\Omega)$ , respectively, we have

$$\langle g, \Lambda_{\sigma} f \rangle = \int_{\Omega} \sigma \nabla u^f \cdot \nabla u^g dx = \langle \Lambda_{\sigma} g, f \rangle;$$

choosing g = f, we get

$$\langle f, \Lambda_{\sigma} f \rangle = \int_{\Omega} \sigma |\nabla u^f|^2 \mathrm{d}x \geqslant 0,$$

and  $\Lambda_{\sigma}f = 0$  if and only if  $u^f = \text{constant}$ , or  $f \in \text{span}\{1\}$ .

Electrode data: To set up a model for the realistic discrete EIT data, model the L electrodes attached to  $\partial\Omega$  as intervals of the boundary curve when n=2, or as connected patches when n=3. Denote the electrodes by  $e_{\ell} \subset \partial\Omega$  and indicate a current pattern applied to them by means of a vector  $J \in \mathbb{R}^L$  whose  $\ell$ th component  $J_{\ell}$  is the net current in the body through the electrode  $e_{\ell}$ . The boundary conditions of the complete electrode model are given by formulas (3), (4) and (5), augmented by the condition (6).

The variational form of the complete electrode model was derived and analyzed in [28], where it was shown that, given an input current vector

$$J \in \mathbb{R}_0^L = \{ X \in \mathbb{R}^L \mid \sum_{\ell=1}^L X_\ell = 0 \},$$

the potential-voltage pair  $(v, V) \in \mathcal{H} = H^1(\Omega) \times \mathbb{R}^L_0$  solves uniquely the variational equation

$$\mathcal{B}((w, W), (v, V)) = \int_{\Omega} \sigma \nabla w \cdot \nabla v dx + \sum_{\ell=1}^{L} \frac{1}{z_{\ell}} \int_{e_{\ell}} (w - W_{\ell})(v - V_{\ell}) dS$$
$$= \sum_{\ell=1}^{L} W_{\ell} J_{\ell}$$
(9)

for all  $(w, W) \in \mathcal{H}$ . The fundamental identity tying together the continuous boundary operator  $\Lambda_{\sigma}$  and the resistance matrix  $R_{\sigma}$  is established in the following theorem.

**Theorem 2.2.** Given  $J \in \mathbb{R}_0^L$  and  $f \in H^{1/2}(\partial\Omega)$ , let  $(v, V) \in \mathcal{H}$  be the solution of the CEM problem with applied current pattern J. Then

$$\int_{\partial\Omega} v \Lambda_{\sigma} f dS + \sum_{\ell=1}^{L} \frac{1}{z_{\ell}} \int_{e_{\ell}} (f - W_{\ell})(v - V_{\ell}) dS - \sum_{\ell=1}^{L} J_{\ell} W_{\ell} = 0, \tag{10}$$

for all  $W \in \mathbb{R}_0^L$ 

П

**Proof.** Let  $u \in H^1(\Omega)$  satisfy the Dirichlet problem with boundary data f. Choosing w = v as a test function in (8), and w = u as a test function in (9), we arrive at the pair of equations

$$\begin{split} &\int_{\Omega} \sigma \nabla v \cdot \nabla u \mathrm{d}x = \int_{\partial \Omega} v \Lambda_{\sigma} f \mathrm{d}S, \\ &\int_{\Omega} \sigma \nabla u \cdot \nabla v \mathrm{d}x = -\sum_{\ell=1}^{L} \frac{1}{z_{\ell}} \int_{e_{\ell}} (f - W_{\ell}) (v - V_{\ell}) \mathrm{d}S + \sum_{\ell=1}^{L} J_{\ell} W_{\ell} \end{split}$$

from which, upon side by side subtraction, the claim follows.

The identity (10) allows us to estimate the boundary data  $(v|_{\partial\Omega}, V) \in H^{1/2}(\partial\Omega) \times \mathbb{R}^L_0$  from the Dirichlet-to-Neumann data, as will be shown in the next section. The converse, namely estimating  $\Lambda_{\sigma}$  from the boundary data (J,V), where the current vector comprises a complete set of current patterns in  $\mathbb{R}^L_0$ , can be interpreted as the corresponding inverse problem. In the next section, we derive a matrix identity formulation of the DtN inverse problem via a discretization of the forward model.

#### 3. Discretization

In the sequel, we assume for simplicity that  $\Omega$  is a unit disc. Generalization to more general domains requires obvious modifications. For the sake of definiteness, we also assume that L, the number of electrodes, is even. To find a computationally feasible approximation of the Dirichlet-to-Neumann map, we define the Sobolev norm in  $H^{1/2}(\partial\Omega)$  in terms of the Fourier series. Let  $u \in H^{1/2}(\partial\Omega) \subset L^2(\partial\Omega)$ , and

$$u(\theta) = u_0 + \sum_{j=1}^{\infty} (u_j^c \cos j\theta + u_j^s \sin j\theta)$$

$$= \frac{1}{\sqrt{2\pi}} (\sqrt{2\pi}u_0) + \sqrt{\pi} \sum_{j=1}^{\infty} \left( (\sqrt{j}u_j^c) \frac{1}{\sqrt{\pi j}} \cos j\theta + (\sqrt{j}u_j^s) \frac{1}{\sqrt{\pi j}} \sin j\theta \right)$$
(11)

be its real Fourier series expansion. Define the  $H^{1/2}(\partial\Omega)$  inner product

$$(u, v)_{H^{1/2}(\partial\Omega)} = 2\pi u_0 v_0 + \pi \sum_{i=1}^{\infty} j(u_j^c v_j^c + u_j^s v_j^s)$$

with the associated  $H^{1/2}(\partial\Omega)$  norm, and define an orthonormal basis  $\{\varphi_j\}_{j=0}^{\infty}$  of  $H^{1/2}(\partial\Omega)$  with respect to this inner product as

$$\varphi_0(\theta) = \frac{1}{\sqrt{2\pi}}, \quad \varphi_{2j}(\theta) = \frac{1}{\sqrt{\pi j}} \cos j\theta, \quad \varphi_{2j-1}\theta = \frac{1}{\sqrt{\pi j}} \sin j\theta, \quad j = 1, 2, \dots$$
(12)

Then the Fourier series representation (11) of any  $v \in H^{1/2}(\partial\Omega)$  can be written concisely as

$$v = \sum_{j=0}^{\infty} v_j \varphi_j, \quad \text{where} \quad v_j = (\varphi_j, v)_{H^{1/2}}. \tag{13}$$

It follows from the definition of the norm that we have a natural isometry

$$H^{1/2}(\partial\Omega) \to \ell^2, \quad v \mapsto \overline{v},$$

where  $\overline{v} = (v_j)_{j=0}^{\infty}$ . In the sequel, we will use v to represent the function and  $\overline{v}$  to represent the coefficients. Likewise, let  $\{\Phi_m\}_{m=1}^{L-1}$  be an orthonormal basis of  $\mathbb{R}_0^L$ , defined as

$$(\Phi_m)_{\ell} = \sqrt{\frac{(2-\delta_{m,L/2})}{L}}\cos\frac{2\pi}{L}m(\ell-1), \quad 1 \leqslant \ell \leqslant L,$$

for  $1 \leq m \leq L/2$ , and

$$(\Phi_{L/2+m})_{\ell} = \sqrt{\frac{2}{L}} \sin \frac{2\pi}{L} m(\ell-1), \quad 1 \leqslant \ell \leqslant L,$$

for  $1 \le m \le L/2 - 1$ . We denote by  $\phi \in \mathbb{R}^{L \times (L-1)}$  the matrix with columns  $\Phi_m, 1 \le m \le L-1$ . To derive a computationally feasible formula to estimate the Dirichlet-to-Neumann map from the resistance map, rearrange (10) to obtain

$$\int_{\partial\Omega} \left( \Lambda_{\sigma} f + \sum_{\ell=1}^{L} \frac{\chi_{\ell}}{z_{\ell}} (f - W_{\ell}) \right) v dS - \sum_{\ell=1}^{L} \left( \frac{1}{z_{\ell}} \int_{e_{\ell}} (f - W_{\ell}) dS \right) V_{\ell} = \sum_{\ell=1}^{L} W_{\ell} J_{\ell}, \tag{14}$$

where  $\chi_{\ell}$  is the characteristic function of the  $\ell$ th electrode, and denote by  $|e_{\ell}|$  its length.

Expressing the voltage potential v in the orthonormal basis (13) and the voltage potential as

$$V = \sum_{m=1}^{L-1} \alpha_m \Phi_m = \Phi \alpha, \tag{15}$$

in (14), we obtain the identity

$$\sum_{j=0}^{\infty} v_j \int_{\partial \Omega} \left( \Lambda_{\sigma} f + \sum_{\ell=1}^{L} \frac{\chi_{\ell}}{z_{\ell}} (f - W_{\ell}) \right) \varphi_j dS - \sum_{m=1}^{L-1} \alpha_m \left( \sum_{\ell=1}^{L} \frac{\Phi_{\ell m}}{z_{\ell}} \int_{e_{\ell}} (f - W_{\ell}) dS \right) = W^{\mathsf{T}} J.$$

It follows from the linearity that this identity holds if and only if it holds for the basis vectors for f and W. Letting  $(f, W) = (\varphi_k, 0)$  we get

$$\sum_{j=0}^{\infty} v_j \int_{\partial\Omega} \left( \Lambda_{\sigma} \varphi_k + \sum_{\ell=1}^{L} \frac{\chi_{\ell}}{z_{\ell}} \varphi_k \right) \varphi_j dS - \sum_{m=1}^{L-1} \alpha_m \left( \sum_{\ell=1}^{L} \frac{\Phi_{\ell m}}{z_{\ell}} \int_{e_{\ell}} \varphi_k dS \right) = 0, \quad 0 \leqslant k < \infty,$$
(16)

while letting  $(f, W) = (0, \Phi_q)$  we obtain

$$-\sum_{j=0}^{\infty} v_j \left( \sum_{\ell=1}^{L} \frac{\Phi_{\ell q}}{z_{\ell}} \int_{e_{\ell}} \varphi_j \mathrm{d}S \right) + \sum_{m=1}^{L-1} \alpha_m \sum_{\ell=1}^{L} \frac{|e_{\ell}|}{z_{\ell}} \Phi_{\ell m} \Phi_{\ell q} = J^{\mathsf{T}} \Phi_q, \quad 1 \leqslant q \leqslant L - 1. \quad (17)$$

To express this set of equations in matrix-vector form, introduce a diagonal matrix  $D \in \mathbb{R}^{L \times L}$ ,

$$\mathsf{D}_{\ell\ell} = rac{|e_\ell|}{z_\ell}, \quad 1 \leqslant \ell \leqslant L,$$

a matrix Y with entries

$$\mathsf{Y}_{j\ell} = \frac{1}{|e_{\ell}|} \int_{e_{\ell}} \varphi_{j} \mathrm{d}S, \quad 1 \leqslant \ell \leqslant L, \quad 0 \leqslant j < \infty,$$

and a matrix M with entries

$$\mathsf{M}_{jk} = \sum_{\ell=1}^{L} \frac{1}{z_{\ell}} \int_{e_{\ell}} \varphi_{j} \varphi_{k} \mathrm{d}S, \quad 0 \leqslant j, k < \infty.$$

Defining the matrix form of the Dirichlet-to-Neumann map as the the array with entries

$$(\mathsf{L}_\sigma)_{jk} = \int_{\partial\Omega} \varphi_j \Lambda_\sigma \varphi_k \mathrm{d}S = \langle \varphi_j, \Lambda_\sigma \varphi_k \rangle, \quad 0 \leqslant j, k < \infty,$$

we can express (16) and (17) compactly as the infinite dimensional symmetric linear system of the form

$$\mathsf{T}\begin{bmatrix} \overline{v} \\ \alpha \end{bmatrix} = \begin{bmatrix} 0 \\ \phi^{\mathsf{T}} J \end{bmatrix}, \quad \mathsf{T} = \begin{bmatrix} \mathsf{L}_{\sigma} + \mathsf{M} & -\mathsf{Y} \mathsf{D} \phi \\ -(\mathsf{Y} \mathsf{D} \phi)^{\mathsf{T}} & \phi^{\mathsf{T}} \mathsf{D} \phi \end{bmatrix}. \tag{18}$$

For more insight in the system (18), we prove some technical results. We start with a modification of the standard trace theorem.

**Lemma 3.1.** For any  $u \in H^1(\Omega)$  satisfying the condition

$$\int_{\partial\Omega} u dS = 0, \tag{19}$$

there is a constant C > 0 such that

$$||u||_{H^{1/2}(\partial\Omega)}^2 \leqslant C \int_{\Omega} |\nabla u|^2 \mathrm{d}x. \tag{20}$$

**Proof.** The result follows from the standard trace theorem and the  $L^2$ -norm of the gradient defines an equivalent Sobolev norm for functions with zero mean trace on the boundary, see, e.g. [22] and references therein. For the sake of completeness, we give a brief proof based on standard references in literature.

If the claim does not hold, for every k = 1, 2, ..., we find a  $u^k \in H^1(\Omega)$  satisfying (19), such that

$$||u^k||_{H^{1/2}(\partial\Omega)}^2 = 1, \quad \int_{\Omega} |\nabla u^k|^2 dx < \frac{1}{k}.$$
 (21)

Denoting the mean value of  $u^k$  over  $\Omega$  by

$$u_{\Omega}^{k} = \frac{1}{|\Omega|} \int_{\Omega} u^{k} \mathrm{d}x,$$

it follows from the Poincaré–Friedrichs inequality ([9], theorem 5.8.1) that there is a constant  $C_1 > 0$  such that

$$||u^k - u_{\Omega}^k||_{L^2(\Omega)}^2 \le C_1 \int_{\Omega} |\nabla u^k|^2 dx$$
 (22)

for all k. From the standard trace theorem in  $H^1(\Omega)$  [11], there is a constant  $C_2$  such that

$$\|u^k - u_{\Omega}^k\|_{H^{1/2}(\partial\Omega)}^2 \leqslant C_2 \|u^k - u_{\Omega}^k\|_{H^1(\Omega)}^2 \leqslant C_2 (\|u^k - u_{\Omega}^k\|_{L^2(\Omega)}^2 + \int_{\Omega} |\nabla u^k|^2 dx),$$

so from (22):

$$||u^k - u_{\Omega}^k||_{H^{1/2}(\partial\Omega)}^2 \le C_2(1 + C_1) \int_{\Omega} |\nabla u^k|^2 dx < \frac{C_2(1 + C_1)}{k},$$

implying that  $(u^k - u_{\Omega}^k)|_{\partial\Omega} \to 0$  in  $H^{1/2}(\partial\Omega)$ , and therefore in  $L^2(\partial\Omega)$ . On the other hand, since the functions  $u^k$  satisfy (19), we have by the Cauchy–Schwarz inequlity:

$$|u_{\Omega}^k| = \frac{1}{|\partial\Omega|} \left| \int_{\partial\Omega} (u^k - u_{\Omega}^k) \mathrm{d}S \right| \leqslant \frac{1}{|\partial\Omega|^{1/2}} \|u^k - u_{\Omega}^k\|_{L^2(\partial\Omega)} \to 0.$$

Finally,

$$||u^k||_{L^2(\Omega)} \le ||u^k - u_{\Omega}^k||_{L^2(\Omega)} + |\Omega|^{1/2} |u_{\Omega}^k| \to 0,$$

and hence, by (21),  $||u^k||_{H^1(\Omega)} \to 0$ . But then, it follows from the trace theorem that

$$1 = \|u^k\|_{H^{1/2}(\partial\Omega)}^2 \leqslant C_2 \|u^k\|_{H^1(\Omega)}^2 \to 0,$$

which is a contradiction, hence proving the lemma.

We are now ready to prove that the sum of the matrices M and  $L_{\sigma}$  defines an isomorphism from  $\ell^2$  to  $\ell^2$ .

**Theorem 3.2.** The infinite matrices M and  $L_{\sigma}$  define continuous linear mappings  $\ell^2 \to \ell^2$ . Furthermore, the mapping  $M + L_{\sigma} : \ell^2 \to \ell^2$  is self-adjoint and bounded from below, therefore invertible.

**Proof.** We start by proving that  $L_{\sigma}$  is bounded. Denoting the  $\ell^2$  inner product by  $(\cdot, \cdot)_{\ell^2}$ , for  $\overline{\nu} \in \ell^2$ , we have that

$$\begin{split} \|\mathsf{L}_{\sigma}\overline{v}\|_{\ell^{2}} &= \sup_{\|\overline{u}\|_{\ell^{2}=1}} \left| (\overline{u}, \mathsf{L}_{\sigma}\overline{v})_{\ell^{2}} \right| \\ &= \sup_{\|\overline{u}\|_{\ell^{2}=1}} \left| \sum_{k=1}^{\infty} \sum_{j=1}^{\infty} u_{k} v_{j} \langle \varphi_{k}, \Lambda_{\sigma} \varphi_{j} \rangle \right| \\ &= \sup_{\|u\|_{H^{1/2}=1}} \left| \langle u, \Lambda_{\sigma} v \rangle \right| \\ &= \|\Lambda_{\sigma} v\|_{H^{-1/2}}, \end{split}$$

and in light of the isometry between  $H^{1/2}$  and  $\ell^2$ :

$$\|\mathsf{L}_{\sigma}\|_{\ell^2 \to \ell^2} = \|\Lambda\|_{H^{1/2} \to H^{-1/2}},$$

showing that  $L_{\sigma}$  is bounded.

Similarly, to show the boundedness of M, we begin by observing that for  $\bar{v} \in \ell^2$ :

$$(\mathsf{M}\overline{v})_k = \sum_{\ell=1}^L \frac{1}{z_\ell} \int_{e_\ell} \varphi_k v \mathrm{d}S = \int_{\partial\Omega} \varphi_k m v \mathrm{d}S,$$

where the function m is given by

$$m = \sum_{\ell=1}^{L} \frac{1}{z_{\ell}} \chi_{\ell},\tag{23}$$

 $\chi_\ell$  being the characteristic function of the  $\ell$ th electrode. Therefore, as above, we have

$$\begin{aligned} |(\overline{u}, \mathsf{M}\overline{v})_{\ell^{2}}| &= \left| \int_{\partial\Omega} u m v \mathrm{d} S \right| \leqslant ||m||_{L^{\infty}} ||u||_{L^{2}} ||v||_{L^{2}} \\ &\leqslant ||m||_{L^{\infty}} ||u||_{H^{1/2}} ||v||_{H^{1/2}} \\ &= ||m||_{L^{\infty}} ||\overline{u}||_{\ell^{2}} ||\overline{v}||_{\ell^{2}}, \end{aligned}$$

implying that  $M:\ell^2\to\ell^2$ , and  $\|M\|_{\ell^2\to\ell^2}\leqslant \|m\|_{L^\infty}=1/\min(z_\ell)$ . The self-adjointness of  $L_\sigma+M$  follows from the self-adjointness of M and  $L_\sigma$ . To show that the mapping is bounded from below, let  $\bar{v} \in \ell^2$  and write

$$v = \sum_{j=0}^{\infty} v_j \varphi_j = v_0 \varphi_0 + \sum_{j=1}^{\infty} v_j \varphi_j = v^0 + v',$$

where  $v^0$  is a constant function, hence by theorem 2.1,  $v^0 \in \mathcal{N}(\Lambda_\sigma) \perp \mathcal{R}(\Lambda_\sigma)$ . Therefore

$$\Lambda_{\sigma}v = \Lambda_{\sigma}v' \perp \varphi_0,$$

hence

$$(\overline{v}, (\mathsf{L}_{\sigma} + \mathsf{M})\overline{v})_{\ell^{2}} = \langle v', \Lambda_{\sigma}v' \rangle + \int_{\partial \Omega} mv^{2} dS$$
$$= \langle v', \Lambda_{\sigma}v' \rangle + ||m^{1/2}v||_{L^{2}}^{2}.$$

Further, denoting by  $u' \in H^1(\Omega)$  the solution of (1) with Dirichlet boundary value  $u'|_{\partial\Omega} = v'$ , we have

$$\langle v', \Lambda_{\sigma} v' \rangle = \int_{\Omega} \sigma |\nabla u'|^2 \mathrm{d}x.$$

Since the integral of v' over the boundary vanishes, it follows from lemma 3.1 that

$$\begin{split} (\overline{v}, (\mathsf{L}_{\sigma} + \mathsf{M}) \overline{v})_{\ell^{2}} &= \int_{\Omega} \sigma |\nabla u'|^{2} \mathrm{d}x + \|m^{1/2}v\|_{L^{2}}^{2} \\ &\geqslant \frac{\sigma_{m}}{C} \|v'\|_{H^{1/2}(\partial \Omega)}^{2} + \|m^{1/2}v\|_{L^{2}}^{2} \\ &= c \|\overline{v}'\|_{\ell^{2}}^{2} + \|m^{1/2}v\|_{L^{2}}^{2}, \end{split}$$

where  $c = \sigma_m/C$ . Next we prove by contradiction that for some constant  $\gamma > 0$ :

$$c\|\overline{v}'\|_{\ell^2}^2 + \|m^{1/2}v\|_{L^2}^2 \geqslant \gamma\|v\|_{H^{1/2}}^2$$
.

If the bound were not true, there is a sequence  $(v^k)$  of functions such that  $||v^k||_{H^{1/2}} = 1$ , and

$$c\|(\overline{v}^k)'\|_{\ell^2}^2 + \|m^{1/2}v^k\|_{L^2}^2 < \frac{1}{k},$$

hence  $\|(\overline{v}^k)'\|_{\ell^2}^2 \to 0$ . In light of the isometry property

$$1 = \|v^k\|_{H^{1/2}}^2 = (v_0^k)^2 + \underbrace{\|(\overline{v}^k)'\|_{\ell^2}^2}_{\to 0},$$

implying that  $(v_0^k)^2 \to 1$  as  $k \to \infty$ , hence  $v^k \to 1$  in  $H^{1/2}(\partial\Omega)$  and hence in  $L^2(\partial\Omega)$ , as  $k \to \infty$ . But since

$$\int_{\partial\Omega} m \mathrm{d}S = \lim_{k \to \infty} \|m^{1/2} v^k\|_{L^2}^2$$

$$\leqslant \lim_{k \to \infty} \left( c \|(\overline{v}^k)'\|_{\ell^2}^2 + \|m^{1/2} v^k\|_{L^2}^2 \right) = 0,$$

then m = 0, contradicting the definition (23) and completing the proof.

It is straightforward to verify that the matrix Y defines a continuous map  $\mathbb{R}^L \to \ell^2$ , therefore, by theorem 3.2, the matrix T defined in (18) defines a continuous map

$$\mathsf{T}:\ell^2\times\mathbb{R}^{L-1}\to\ell^2\times\mathbb{R}^{L-1}\quad\text{where}\quad \mathsf{T}=\begin{bmatrix} \mathsf{L}_\sigma+\mathsf{M} & -\mathsf{Y}\mathsf{D}\varphi\\ -(\mathsf{Y}\mathsf{D}\varphi)^\mathsf{T} & \varphi^\mathsf{T}\mathsf{D}\varphi \end{bmatrix}.$$

We are now ready to prove the main result of this section, establishing the connection between the Dirichlet-to-Neumann map and the resistance map.

**Theorem 3.3.** The matrices  $L_{\sigma}: \ell^2 \to \ell^2$  and  $R_{\sigma} \in \mathbb{R}^{L \times L}$  satisfy the identity

$$\phi^{\mathsf{T}} \mathsf{D} \phi - (\mathsf{Y} \mathsf{D} \phi)^{\mathsf{T}} (\mathsf{L}_{\sigma} + \mathsf{M})^{-1} \mathsf{Y} \mathsf{D} \phi = \widetilde{\mathsf{R}}_{\sigma}^{-1}, \tag{24}$$

where  $\widetilde{R}_{\sigma}$  is the representation of the resistance map in the basis  $\phi$ :

$$\widetilde{\mathsf{R}}_{\sigma} = \boldsymbol{\Phi}^{\mathsf{T}} \mathsf{R}_{\sigma} \boldsymbol{\Phi} \in \mathbb{R}^{(L-1) \times (L-1)}$$
.

**Proof.** If follows from the invertibility of the operator  $L_{\sigma} + M$  that we can solve the first block of (18) for  $\overline{v}$ :

$$\overline{v} = (\mathsf{L}_{\sigma} + \mathsf{M})^{-1} \mathsf{YD} \varphi \alpha,$$

and substituting this expression in the second block we obtain the following equation in terms of the Schur complement of a block of the matrix T:

$$\left(\phi^{\mathsf{T}}\mathsf{D}\phi - (\mathsf{Y}\mathsf{D}\phi)^{\mathsf{T}}\left(\mathsf{L}_{\sigma} + \mathsf{M}\right)^{-1}\mathsf{Y}\mathsf{D}\phi\right)\alpha = \phi^{\mathsf{T}}J. \tag{25}$$

It follows from

$$V = \Phi \alpha = R_{\sigma} J$$

and the orthonormality of the vectors  $\Phi_{\ell}$  that

$$\alpha = \Phi^{\mathsf{T}} \Phi \alpha = \Phi^{\mathsf{T}} \mathsf{R}_{\sigma} J.$$

Letting  $J = \Phi_m$ ,  $1 \le m \le L - 1$  in (25) we have that

$$\left(\varphi^\mathsf{T} \mathsf{D} \varphi - (\mathsf{Y} \mathsf{D} \varphi)^\mathsf{T} \left(\mathsf{L}_\sigma + \mathsf{M}\right)^{-1} \mathsf{Y} \mathsf{D} \varphi\right) \varphi^\mathsf{T} \mathsf{R}_\sigma \varphi = \mathsf{I}_{\mathit{L}-1},$$

where  $I_{L-1}$  is the unit matrix of size  $(L-1) \times (L-1)$ . The claim of the theorem follows from this identity.

Using the notation of Schur complements and referring to the blocks of the matrix T in (18) by  $T^{ij}$ , the result can be written concisely as

$$T/T^{11} = \widetilde{R}_{\sigma}^{-1}$$

where

$$\mathsf{T}/\mathsf{T}^{11} = \varphi^\mathsf{T} \mathsf{D} \varphi - (\mathsf{Y} \mathsf{D} \varphi)^\mathsf{T} \left(\mathsf{L}_\sigma + \mathsf{M}\right)^{-1} \mathsf{Y} \mathsf{D} \varphi.$$

In the computed examples we approximate the operator  $M + L_{\sigma}$  and its inverse by their truncated finite dimensional approximations. Since these operators are invertible, therefore not compact, convergent low rank approximations are not guaranteed. However, the even rows of the matrix Y are given by

$$\mathsf{Y}_{2j,\ell} = \frac{1}{|e_{\ell}|} \int_{e_{\ell}} \varphi_{2j} \mathrm{d}S = \frac{1}{\sqrt{\pi j}} \frac{1}{|e_{\ell}|} \int_{e_{\ell}} \cos j\theta \mathrm{d}\theta = \frac{1}{\sqrt{j}} \widehat{\mathsf{Y}}_{2j,\ell},$$

and in the odd rows are

$$\mathsf{Y}_{2j-1,\ell} = \frac{1}{|e_{\ell}|} \int_{e_{\ell}} \varphi_{2j-1} \mathrm{d}S = \frac{1}{\sqrt{\pi j}} \frac{1}{|e_{\ell}|} \int_{e_{\ell}} \sin j\theta \mathrm{d}\theta = \frac{1}{\sqrt{j}} \widehat{\mathsf{Y}}_{2j-1,\ell}.$$

Hence, introducing the diagonal matrix H:

$$\mathsf{H}_{00} = 1, \mathsf{H}_{2j,2j} = \mathsf{H}_{2j-1,2j-1} = \frac{1}{\sqrt{j}},$$

we have

$$\left(\mathsf{Y}\mathsf{D}\varphi\right)^\mathsf{T}\left(\mathsf{L}_\sigma+\mathsf{M}\right)^{-1}\mathsf{Y}\mathsf{D}\varphi=\left(\widehat{\mathsf{Y}}\mathsf{D}\varphi\right)^\mathsf{T}\left[\mathsf{H}^\mathsf{T}\left(\mathsf{L}_\sigma+\mathsf{M}\right)^{-1}\mathsf{H}\right]\widehat{\mathsf{Y}}\mathsf{D}\varphi.$$

The operator  $H: \ell^2 \to \ell^2$  is compact, and therefore, so is  $H^T(L_{\sigma} + M)^{-1}H$ , allowing convergent low rank approximations.

Finally, we point out that since the operator  $\widehat{\mathsf{Y}}\mathsf{D}\varphi:\ell^2\to\mathbb{R}^{L-1}$  has rank L-1, we do not expect to be able to recover reliably much more than Fourier modes of order L/2, as the computed examples confirm.

#### 4. Inverse problem of estimating $L_{\sigma}$

In this section, we propose a computational approach based on the Bayesian paradigm to estimate in a stable way the matrix of the Dirichlet-to-Neumann map from the measured resistance map. To design a meaningful prior for the unknown matrix that we want to estimate, we generate a representative sample of plausible Dirichlet-to-Neumann matrices, extract the principal feature vectors of the sample and reduce the complexity of the problem by a procedure analogous to that applied for principal component analysis (PCA) [18]. Similar ideas were previously used in [5, 6] where part of the inverse problem was to estimate the Dirichlet-to-Neumann map, or the Poincaré-Steklov operator, on an inaccessible fictitious domain boundary.

#### 4.1. Sample-based prior and model reduction

Using the trigonometric basis (12), we approximate the exact Dirichlet-to-Neumann matrix by an  $(n + 1) \times (n + 1)$  truncated matrix: assuming that n is even so that we have equal number of sines and cosines, we partition the finite matrix approximation  $L^n_{\sigma}$  of  $L_{\sigma}$  as

$$\mathsf{L}_{\sigma}^{n} = \begin{bmatrix} 0 & \mathsf{0}_{n \times 1} \\ \mathsf{0}_{n \times 1} & \widetilde{\mathsf{L}}_{\sigma}^{n} \end{bmatrix},\tag{26}$$

where  $\widetilde{\mathsf{L}}_{\sigma}^n \in \mathbb{R}^{n \times n}$  is symmetric positive definite. The choice of the truncation index n will be discussed in the section where we describe the computed experiments.

To estimate  $L^n_{\sigma}$  from  $R_{\sigma}$  in the Bayesian framework, we assume an *a priori* probability distribution  $\pi_{\sigma}$  for the conductivity  $\sigma$  and generate a representative sample of independently drawn conductivities  $\{\sigma_j\}_{j=1}^K$ . For each  $\sigma_j$ , we compute a numerical approximation of the Dirichlet-to-Neumann map:

$$\sigma_j \mapsto \mathsf{L}^n_{\sigma_j} \in \mathbb{R}^{(n+1)\times (n+1)}, \quad 1 \leqslant j \leqslant K$$

and the corresponding perturbed Neumann-to-Dirichlet matrix:

$$X_{\sigma_j} = \left(M^n + L^n_{\sigma_j}\right)^{-1}, \quad 1 \leqslant j \leqslant K, \tag{27}$$

where  $M^n$  is the  $(n+1) \times (n+1)$  truncated approximation of the infinite matrix M. For notational convenience, we suppress the *n*-dependence of the matrix X. We can extract the most significant feature matrices either from the generated data sample, or from a centralized version of it obtained by removing from each sample matrix the sample mean. In the latter case, we denote the mean of the associated sample of matrices by

$$\overline{\mathsf{X}} = rac{1}{K} \sum_{j=1}^K \mathsf{X}_{\sigma_j},$$

and denote the centered matrices by

$$X_{\sigma_i,c} = X_{\sigma_i} - \overline{X}$$
.

In the following, we assume that the feature matrices are extracted from a centralized sample. The non-centralized case is obtained by simply setting  $\overline{X} = 0$ . Each centered Dirichlet-to-Neumann matrix in the centralized sample can be represented in vector form via the natural isometry

$$\operatorname{vec}: (\mathbb{R}^{(n+1)\times (n+1)}, ||\cdot||_F) \to (\mathbb{R}^{(n+1)^2}, ||\cdot||), \quad \begin{bmatrix} u_0 & u_1 & \cdots & u_n \end{bmatrix} \mapsto \begin{bmatrix} u_0 \\ u_1 \\ \vdots \\ u_n \end{bmatrix},$$

where  $\|\cdot\|_F$  denotes the Frobenius norm of a matrix; we store the corresponding vectors as the columns of the matrix  $\mathscr{X}$ :

$$\mathscr{X} = \begin{bmatrix} \operatorname{vec}(\mathsf{X}_{\sigma_1,c}) & \operatorname{vec}(\mathsf{X}_{\sigma_2,c}) & \cdots & \operatorname{vec}(\mathsf{X}_{\sigma_K,c}) \end{bmatrix} \in \mathbb{R}^{(n+1)^2 \times K},$$

and compute its dominant left singular vectors. Let

$$\mathscr{X} = \mathscr{U}\mathscr{D}\mathscr{V}^\mathsf{T}$$

be the singular value decomposition of  $\mathscr{X}$ , with the convention that the singular values  $\lambda_j$ , which are the diagonal entries of the diagonal matrix  $\mathscr{D}$  appear in non-increasing order. We denote by  $\mathsf{U}_j \in \mathbb{R}^{(n+1)\times (n+1)}$  the matrices corresponding to the columns of the matrix  $\mathscr{U}$ , that is

$$\mathscr{U} = \begin{bmatrix} \operatorname{vec}(\mathsf{U}_1) & \operatorname{vec}(\mathsf{U}_2) & \cdots & \operatorname{vec}(\mathsf{U}_{(n+1)^2}) \end{bmatrix}.$$

We select a threshold value  $\tau > 0$ , and find the index k such that

$$\lambda_k > \tau \geqslant \lambda_{k+1}$$
.

The matrices corresponding to singular values above the threshold  $\tau$  are the principal feature matrices, and for any conductivity  $\sigma$ , we approximate the matrix  $X_{\sigma}$  in terms of the reduced PCA basis  $\{U_j\}_{j=1}^k$  by writing

$$X_{\sigma} \approx \overline{X} + \sum_{j=1}^{k} \beta_{j} U_{j}, \tag{28}$$

where the coefficients  $\beta_j$  are the principal components of  $X_{\sigma}$ . Replacing  $X_{\sigma}$  in (24) by its reduced basis approximation (28) and denoting

$$B = YD\phi$$
,  $C = \phi^T D\phi$ ,

we arrive at the following linear formulation of the problem.

**Problem 4.1.** Given the reduced basis  $\{\overline{X}, U_j\}_{j=1}^k$ , and the observed noisy approximation of the resistance map  $\widetilde{R}_{\sigma}$  in the basis  $\phi$ , estimate the principal components  $\{\beta_j\}_{j=1}^k$  of  $X_{\sigma}$  by solving the equation

$$C - B^{\mathsf{T}} \overline{X} B - \sum_{j=1}^{k} \beta_j B^{\mathsf{T}} U_j B = \widetilde{R}_{\sigma}^{-1}$$
(29)

in the least squares sense.

While the computation of the least squares solution is, in principle, straightforward and provides a way to estimate the matrix  $L^n_{\sigma}$ , a number of algorithmic details need to be carefully addressed in order to attain sufficient accuracy and computational efficiency.

#### 5. Computational details

The forward solution to generate the prior sample of Dirichlet-to-Neumann maps as well as the generation of test data based on the complete electrode model are done using a standard finite element method. Since the selection of parameters in the model depend on the computational details, we briefly summarize the numerical methods in the following subsection.

#### 5.1. Finite element approximation of the DtN matrix

To collect the sample of Dirichlet-to-Neumann matrices from a given conductivity distribution in  $\Omega$ , we first generate a first order triangular finite element mesh over  $\Omega$ , with vertices  $\{z_j\}_{j=1}^N$ . The nodes are arranged so that the first m are boundary nodes, and the remaining N-m are

interior nodes. In the numerical simulations, we use a first order finite element model, denoting by  $\{\psi_j\}_{j=1}^N$  the first order piecewise polynomial nodal basis, that is,  $\psi_j(z_k) = \delta_{jk}$ .

To calculate the finite element approximation of the solution u of the Dirichlet problem (1) and (2), we partition the stiffness matrix  $S \in \mathbb{R}^{N \times N}$ :

$$\mathsf{S}_{jk} = \int_{\Omega} \sigma \nabla \psi_j \cdot \nabla \psi_k \mathrm{d}z, \quad 1 \leqslant j, k \leqslant N, \tag{30}$$

according to whether the index corresponds to a boundary or interior node:

$$\mathsf{S} = \mathsf{S}_{\sigma} = \begin{bmatrix} \mathsf{S}^{11} & \mathsf{S}^{12} \\ \mathsf{S}^{21} & \mathsf{S}^{22} \end{bmatrix}, \quad \mathsf{S}^{11} \in \mathbb{R}^{m \times m}, \; \mathsf{S}^{22} \in \mathbb{R}^{(N-m) \times (N-m)},$$

and denote by  $\gamma \in \mathbb{R}^m$  the vector containing the boundary values:

$$\gamma = \begin{bmatrix} f(z_1) \\ \vdots \\ f(z_m) \end{bmatrix}.$$

The approximation of the solution u in the nodal basis can be written as

$$u = \sum_{j=1}^{N} u_j \psi_j = \sum_{j=1}^{m} \gamma_j \psi_j + \sum_{j=m+1}^{N} u_j \psi_j.$$
 (31)

The standard variational formulation corresponding to the Dirichlet problem given by (8) leads to the well-posed matrix equation

$$S^{22}u_{\rm int} = -S^{21}\gamma,\tag{32}$$

where

$$u_{ ext{int}} = \begin{bmatrix} u_{m+1} \\ \vdots \\ u_N \end{bmatrix} \in \mathbb{R}^{N-m},$$

is the vector containing the nodal values at the interior points.

Let g be a function defined on the boundary  $\partial\Omega$ , with nodal values

$$\rho = \begin{bmatrix} g(z_1) \\ \vdots \\ g(z_m) \end{bmatrix} \in \mathbb{R}^m.$$

We can continue g into the domain  $\Omega$  by defining w to be the lifting of the boundary function:

$$w = \sum_{i=1}^{N} w_i \psi_j = \sum_{i=1}^{m} \rho_i \psi_i,$$
(33)

satisfying  $w(z_i) = g(z_i), 1 \le j \le m$ .

Replacing w and u with their approximate expressions (31) and (33) in terms of  $\{\psi_j\}$  in the right hand side of

$$\int_{\partial\Omega} g\Lambda_{\sigma}fdS = \int_{\Omega} \sigma\nabla w \cdot \nabla udz,$$

using (32) we obtain the numerical approximation

$$\int_{\partial \Omega} g \Lambda_{\sigma} f dS = \rho^{\mathsf{T}} \mathsf{S}^{11} \gamma + \rho^{\mathsf{T}} \mathsf{S}^{12} u_{\mathsf{int}} = \rho^{\mathsf{T}} \left( \mathsf{S}^{11} - \mathsf{S}^{12} \left( \mathsf{S}^{22} \right)^{-1} \mathsf{S}^{21} \right) \gamma = \rho^{\mathsf{T}} (\mathsf{S}/\mathsf{S}^{22}) \gamma.$$

In particular, choosing f and g from the Fourier basis on the boundary, we have

$$(\mathsf{L}_{\sigma}^{n})_{jk} = \gamma_{j}^{\mathsf{T}} \left( \mathsf{S}^{11} - \mathsf{S}^{12} \left( \mathsf{S}^{22} \right)^{-1} \mathsf{S}^{21} \right) \gamma_{k},$$

where

$$\gamma_j = \begin{bmatrix} \varphi_j(z_1) \\ \vdots \\ \varphi_j(z_m) \end{bmatrix}, \quad 1 \leqslant j \leqslant n.$$

Finally, after assembling the trigonometric boundary values into the matrix

$$G = \begin{bmatrix} \gamma_1 & \cdots & \gamma_n \end{bmatrix} \in \mathbb{R}^{m \times n},$$

we obtain a computable approximation for the positive definite part of the Dirichlet-to-Neumann matrix as a Schur complement of the block  $S^{22}$  of the stiffness matrix,

$$\widetilde{L}_{\sigma}^{\mathit{n}} = \mathsf{G}^{\mathsf{T}} \left( \mathsf{S}^{11} - \mathsf{S}^{12} \left( \mathsf{S}^{22} \right)^{-1} \mathsf{S}^{21} \right) \mathsf{G} = \mathsf{G}^{\mathsf{T}} (\mathsf{S}/\mathsf{S}^{22}) \mathsf{G}.$$

Several versions of the FEM implementation of the complete electrode model can be found in the literature, see, e.g. [31–33]. Here, we follow the formalism in [3, 4] using tensor product bases, as outlined below.

Assuming, for simplicity, that the domain  $\Omega$  is discretized into triangular elements corresponding to N nodes, we define the finite element basis for pairs (v, V) as

$$\overline{\psi}_k = (\psi_k, 0), \quad 1 \leqslant k \leqslant N, \quad \overline{\psi}_{N+\ell} = (0, \Phi_\ell), \quad 1 \leqslant \ell \leqslant L - 1$$

and write the Galerkin approximation of the CEM model as

$$(v, V) \approx \sum_{i=1}^{N+L-1} \alpha_i \overline{\psi}_k,$$

leading to the FEM matrix approximation of the variational form:

$$\sum_{i=1}^{N+L-1} \mathscr{B}(\overline{\psi}_k, \overline{\psi}_j) \alpha_j = \begin{cases} 0, & 1 \leqslant k \leqslant N \\ \Phi_\ell^\mathsf{T} J, & k = N+\ell, \ 1 \leqslant \ell \leqslant L-1. \end{cases}$$

Partitioning the matrix  $\mathsf{K} = \left[\mathscr{B}(\overline{\psi}_k, \overline{\psi}_j)\right] \in \mathbb{R}^{(N+L-1)\times(N+L-1)}$  according to whether the coefficients refer to the mesh nodes or the electrodes, we can write the equation as

$$\mathsf{K} = \begin{bmatrix} \mathsf{K}^{11} & \mathsf{K}^{12} \\ \mathsf{K}^{21} & \mathsf{K}^{22} \end{bmatrix} \begin{bmatrix} \alpha^1 \\ \alpha^2 \end{bmatrix} = \begin{bmatrix} 0 \\ \varphi^\mathsf{T} J \end{bmatrix},$$

where the entries of  $\alpha^1 \in \mathbb{R}^N$  are the coefficients defining the voltage potential, while  $\alpha^2$  contains the coefficients of the electrode voltages in the basis  $\{\Phi_\ell\}$ . After one step of Gaussian elimination to find an expression for  $\alpha^1$  in terms of  $\alpha^2$ , we arrive at the following equation for  $\alpha^2$ :

$$\left(\mathsf{K}^{22} - \mathsf{K}^{21} \left(\mathsf{K}^{11}\right)^{-1} \mathsf{K}^{12}\right) \alpha^2 = \Phi^{\mathsf{T}} J$$

from which it follows that the voltage can be expressed as

$$V = \phi \alpha^2 = \phi \left( \mathsf{K}^{22} - \mathsf{K}^{21} \left( \mathsf{K}^{11} \right)^{-1} \mathsf{K}^{12} \right)^{-1} \Phi^\mathsf{T} J = \mathsf{R}_\sigma J.$$

In turn, recalling that  $\phi^T \phi = I_{L-1}$ , the reduced resistance matrix  $\widetilde{R}_{\sigma}$  can be written as

$$\widetilde{\mathsf{R}}_{\sigma} = \left(\mathsf{K}^{22} - \mathsf{K}^{21} \left(\mathsf{K}^{11}\right)^{-1} \mathsf{K}^{12}\right)^{-1},$$

the inverse of the Schur complement  $K/K^{11}$ .

#### 5.2. Prior model and sampling the conductivities

The computation of the basis vectors for the principal components reduced order approximation of the Dirichlet-to-Neumann matrix requires a sample of conductivities, assumed to be independent realizations of an underlying random variable.

To have a finite dimensional parametrization of the conductivity, we define a triangular mesh independent of the finite element meshes used for solving the forward problems. We denote the vertices of the conductivity mesh by  $\zeta_j$ ,  $1 \le j \le M$ , and denote by  $\{\chi_j\}_{j=1}^M$  the first order , or piecewise linear nodal basis associated to this mesh,  $\chi_j(\zeta_k) = \delta_{jk}$ . The prior model used to generate the conductivities is assumed to be of the form

$$\sigma(z) = \sigma_0 \exp\left(W(z) \sum_{j=1}^{M} \xi_j \chi_j(z)\right),$$

where  $\sigma_0$  is the background conductivity, W(z) is a quadratic weight damping the conductivity near the boundary,  $W(z) = 1.1 - |z|^2$ , and the coefficient vector  $\xi \in \mathbb{R}^M$  is drawn from a Whittle–Mátern type correlation prior model [24, 25] described as follows: if  $A \in \{0, 1\}^{M \times M}$  denotes the adjacency matrix of the graph defined by the nodes and edges of the conductivity mesh, we define the graph Laplacian  $\Delta_g \in \mathbb{R}^{M \times M}$  as

$$\Delta_g = \frac{1}{h^2} \left( \mathsf{A} - \operatorname{diag} \left( \mathsf{A} E_M \right) \right),\,$$

where  $E_M \in \mathbb{R}^M$  is a vector of ones, and h > 0 is a parameter approximating the mean distance between the nodes. The vectors  $\xi$  are obtained by solving the system

$$\beta \lambda \left( \Delta_g - \lambda^{-2} \mathsf{I}_M \right) \xi = w, \quad w \sim \mathcal{N}(0, \mathsf{I}_M), \tag{34}$$

where  $\beta > 0$  is a scaling factor,  $\lambda > 0$  is the correlation length and  $I_M$  is the  $M \times M$  identity matrix, and the vectors w are drawn independently for each realization. We point out that the damping term W reduces the *a priori* variance of the conductivity at the boundary. Since the Dirichlet-to-Neumann map is most sensitive to conductivity near the boundary, the variance reduction has a regularizing effect on the inverse problem of estimating the map, as discussed later

#### 6. Computed examples

In our numerical experiments, we assume that the domain  $\Omega$  is the unit disc with L=16 identical equally spaced electrodes attached to the boundary with space filling ratio 0.7. The contact impedance is assumed to be the same at each electrode,  $z_{\ell}=0.1$ . The finite element

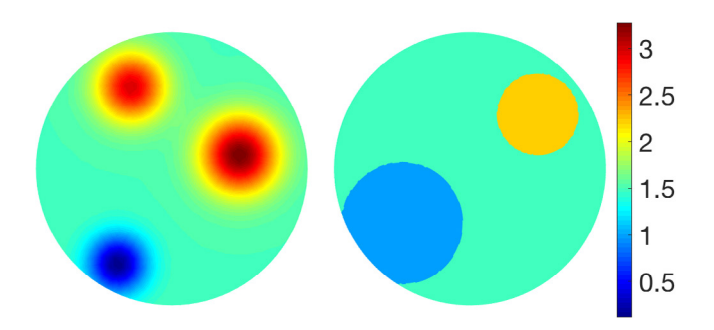


**Figure 1.** Two conductivity distributions used in the computed examples. The conductivity on the left comprises three Gaussian inclusions, corresponding to the prior model that assumes smoothness, while the one on the left is not in line with the prior assumptions.

computations are done using a first order basis on triangular meshes generated with the DistMesh generator, [23]. To avoid the inverse crime, the resistance matrices  $R_{\sigma}$  simulating the measured data are computed using a mesh with  $n_{\nu}=3678$  vertices and  $n_{e}=7018$  elements, with 336 boundary nodes, while the Dirichlet-to-Neumann maps constituting the sample used to extract the principal feature matrices are computed in a slightly coarser mesh with  $n_{\nu}=3225$  vertices and  $n_{e}=6128$  elements, corresponding to 320 boundary nodes.

We start by considering the error in the matrix equation (24) due to the truncation of the Fourier basis with two conductivity distributions, a constant conductivity  $\sigma = \sigma_0 = 1.5$ , and a smooth conductivity  $\sigma = \sigma_{smooth}$  with three Gaussian perturbations on constant background, shown on the left in figure 1. Observe that for the constant conductivity, the Dirichlet-to-Neumann matrix in the Fourier basis is analytically known:

$$\mathsf{L}_{\sigma_0}^n = \sigma_0 \operatorname{diag}(0, 1, 1, \dots, 1) \in \mathbb{R}^{(n+1) \times (n+1)}. \tag{35}$$

For the non-constant conductivity matrix, we need to resort to a numerical approximation. We address the following question: given the FEM grid, in this case the coarser grid, how should n be chosen? Clearly, the density of the computational mesh sets an upper bound for n: if  $n_b$  is the number of boundary nodes, the Nyquist sampling theorem suggests that the highest frequency n/2 of the Fourier modes on the boundary should not exceed  $n_b/2$ , that is,  $n \le n_b$ . On the other hand, if n is too small, the truncation error may render the matrix equation (24) inaccurate, and the modeling error starts to dominate over noise in the data.

In the first numerical test, for each n = 1, 2, ..., we compute the matrices  $Y = Y^n$  and  $M = M^n$  analytically, and consider the relative error

$$E_n = \frac{\|\phi^\mathsf{T} \mathsf{D}\phi - (\mathsf{Y}^n \mathsf{D}\phi)^\mathsf{T} (\mathsf{L}^n_\sigma + \mathsf{M}^n)^{-1} \mathsf{Y}^n \mathsf{D}\phi - \widetilde{\mathsf{R}}^{-1}_\sigma \|_F}{\|\widetilde{\mathsf{R}}^{-1}_\sigma\|_F},\tag{36}$$

where  $L^n_\sigma$  is either the analytically known or numerically computed truncated Dirichlet-to-Neumann matrix, and  $\widetilde{R}_\sigma$  is computed using the finer mesh; this would correspond to measured noiseless quantities. Figure 2 shows the approximation errors for constant conductivity  $\sigma_0$  (left panel) and non-constant smooth conductivity  $\sigma_{\text{smooth}}$  (right panel). Interestingly, the modeling error curves with the constant conductivity and the variable one have a similar shape when the Dirichlet-to-Neumann matrices  $L^n_\sigma$  are computed numerically. In the case where the analytic expression for the matrix is available, the accuracy is a little higher around n=80. Observe, that in both cases the modeling error is not monotonically decreasing with n, but it

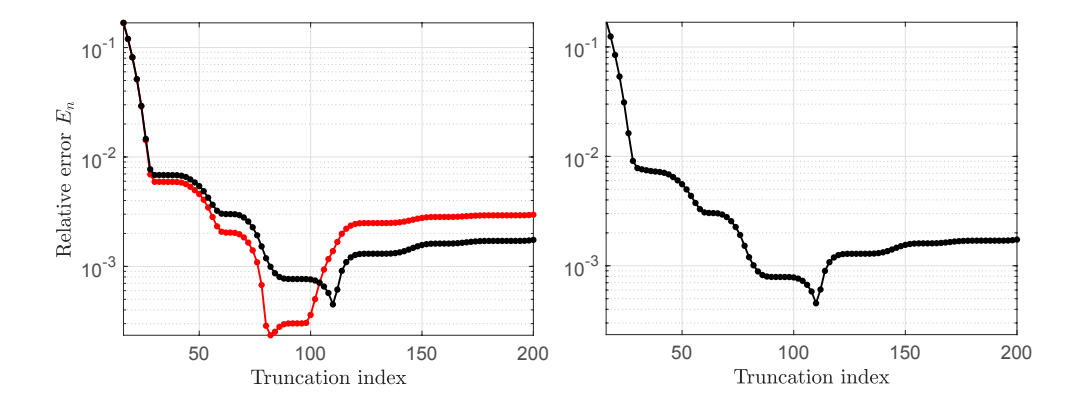


Figure 2. The error (36) in the matrix identity (24) relative to the presumably known conductance matrix  $\widetilde{\mathsf{R}}_\sigma^{-1}$  that is approximated numerically using a finer FEM mesh than that used to compute the Dirichlet-to-Neumann matrix. The abscissa indicates the truncation level of the Fourier series approximation of the boundary voltages. Left: constant conductivity  $\sigma=1.5$ , the black curve corresponding to the numerically computed approximation of the Dirichlet-to-Neumann matrix, the red one to the analytic expression. Right: smooth conductivity  $\sigma_{smooth}$  shown in figure 1. The Dirichlet-to-Neumann map is computed using the coarser mesh shown in figure 3.

starts to grow around n = 110 or earlier around n = 100 in the case of the analytically computed solution (red curve in the left panel of figure 2). This phenomenon may be due to the fact that in our computations the resistance matrix is not analytically known, and we have to use a numerical approximation. In light of this observations, we set n = 110.

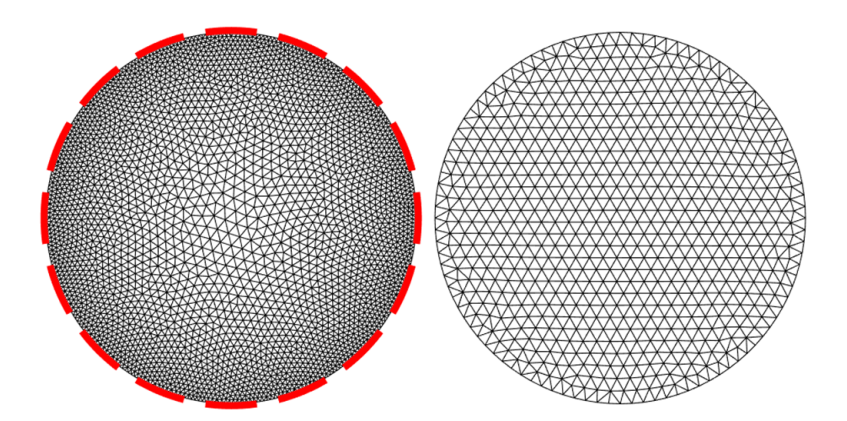
Keeping n=110 fixed, we generate a sample of random conductivities according to the procedure described in the previous section. The conductivities drawn from the prior are computed in a homogeneous mesh. For the FEM computations, the nodal values of the vector  $\xi = \log(\sigma/\sigma_0)$  are interpolated linearly to Gauss quadrature points of the FEM mesh for the computation of the stiffness matrices. The coarser FEM mesh as well as the mesh used for representing the conductivities are shown in figure 3.

Figure 4 shows some of the randomly generated conductivities. Because our sample size K = 5000 is rather small, we do not expect this sample to be representative of the conductivities, however since the Dirichlet-to-Neumann map is not sensitive to details in the conductivity, in itself a source of the ill-posedness of the EIT inverse problem, we may have a good chances to capture the main features of the boundary matrices with a relatively small sample.

Once the sample has been produced, we compute the singular value decomposition for the data set. Figure 5 shows the singular values of the non-centered sample matrix  $\mathscr{X}$ , normalized to have the largest singular value equal to one. We observe that the singular values decrease rapidly by several orders of magnitude, however, there is no clear spectral gap suggesting an obvious value where to truncate.

To better understand the resolution power of the singular vectors, we consider how much the matrices  $X_{\sigma}$  corresponding to different conductivities differ from their orthogonal projections to the affine subspaces  $Q_k = \overline{X} + \operatorname{span}\{U_1, \ldots, U_k\}$  where we search for the approximate solution. More precisely, if  $L_{\sigma}^n \in \mathbb{R}^{(n+1)\times (n+1)}$  is a numerical approximation of the Dirichlet-to-Neumann matrix of a known conductivity, we compute the orthogonal projections

$$\widehat{\beta} = \mathscr{U}^{\mathsf{T}} \operatorname{vec}(\mathsf{X}_{\sigma} - \overline{\mathsf{X}}), \quad \mathsf{X}_{\sigma} = (\mathsf{M}^n + \mathsf{L}_{\sigma}^n)^{-1},$$



**Figure 3.** Left: The FEM coarse mesh used for solving the forward problem to generate the Dirichlet-to-Neumann sample. Right: The regular mesh in which the conductivities are generated. The nodal values of the logarithmic conductivities are linearly interpolated to the Gauss quadrature points in each element of the FEM mesh.

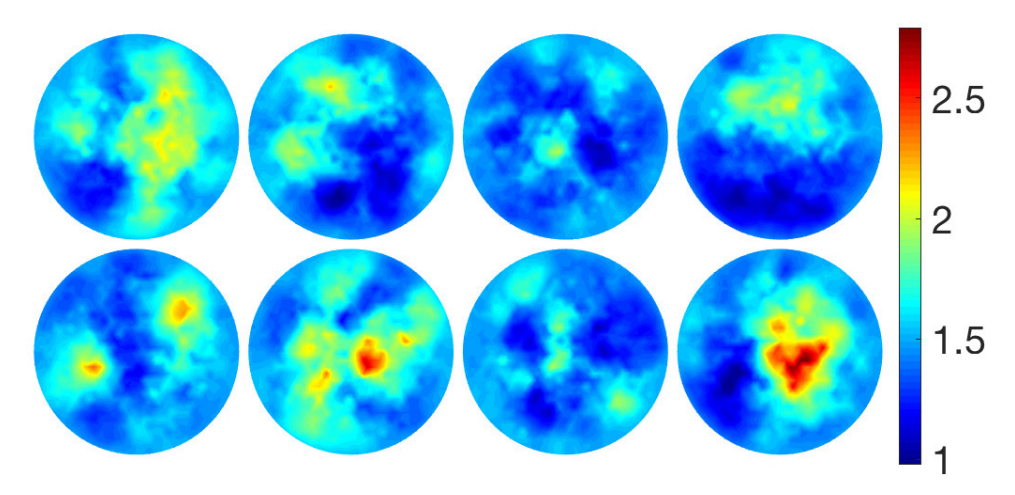


**Figure 4.** Eight random conductivities: the nodal values of the piecewise linear quantity  $\xi = \log \sigma/\sigma_0$  are drawn from the to a Whittle–Mátern correlation prior with correlation length  $\lambda = 0.2$  and scaling factor  $\beta = 1/15$ .

and the corresponding approximation error

$$e_k = \frac{\|\mathsf{X}_{\sigma} - \overline{\mathsf{X}} - \sum_{j=1}^k \widehat{\beta}_j \mathsf{U}_j\|_F}{\|\mathsf{X}_{\sigma}\|_F}$$
(37)

for different truncation levels k. This is a lower bound for the actual error when computing the approximation using the resistance map.

Figure 6 shows the approximation errors as a function of the truncation index k for the constant conductivity  $\sigma_0 = 1.5$  and the smooth non-homogeneous conductivity  $\sigma_{\text{smooth}}$  shown in figure 1 (left). In our test, we used the non-centered sample, that is,  $\overline{X} = 0$ . The relative truncation error depends on how the Dirichlet-to-Neumann matrix is computed. In the constant conductivity case, we use either the analytical formula (35), or the FEM-based approximation using either the mesh used to generate the sample (labeled 'coarse mesh'), or the dense mesh

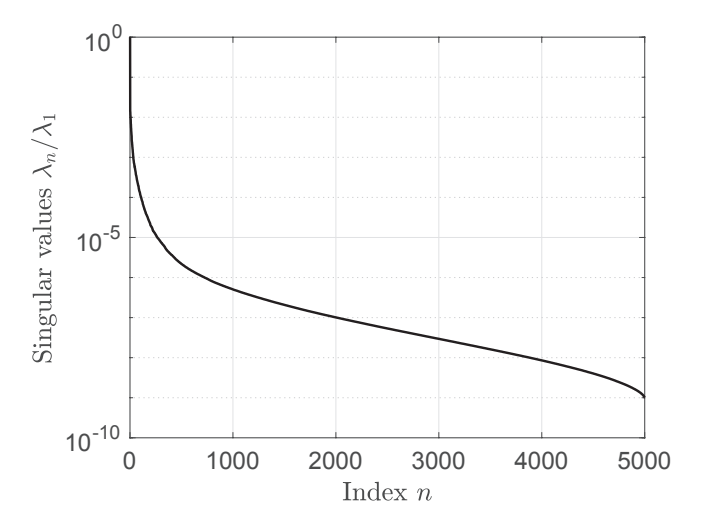


Figure 5. The singular values of the sample matrix, scaled by the largest singular values.

used to generate the data (labeled 'dense mesh'). We observe, as to be expected, that if the Dirichlet-to-Neumann matrix is approximated using the same mesh used for the generation of the sample, the approximation error is smaller than for the dense mesh approximation or when the matrix is analytically available. The results for the smooth conductivity example are similar, although in that case the analytic formula is not available.

Finally, we test how well the Dirichlet-to-Neumann matrix can be approximated based on the given conductance matrix by solving the least squares problem (29) for the coefficients  $\beta_j$  and further estimating  $L^n_\sigma$  from the approximation of the matrix  $X_\sigma$ . We consider three cases, the constant conductivity, the smooth conductivity, and a discontinuous conductivity, shown in figure 1 (right), for which the sample of smooth conductivities is not representative.

Given a truncation index k, we solve equation (29) in the least squares sense to find the coefficients  $\beta_1, \ldots, \beta_k$  and write the corresponding approximation:

$$\widehat{\mathsf{X}}^k = \overline{\mathsf{X}} + \sum_{j=1}^k \beta_k \mathsf{U}_k,$$

and further compute

$$\widehat{\mathsf{L}}_{\sigma}^{n,k} = (\widehat{\mathsf{X}}^k)^{-1} - \mathsf{M}^n. \tag{38}$$

Observe that here the truncation index k acts as a regularization, similarly as in the truncated SVD regularization for linear ill-posed problems, therefore the choice of k is a trade-off between how small we want the residual to be versus how much error the solution tolerates. The error in the model (29) consists of the numerical error in the data and the modeling error due to the finite approximation, including the errors due to the FEM computations. As pointed out earlier, the modeling error at the truncation level n = 110 is of the order of magnitude  $\sim 10^{-3}$  of the data, measured in the Frobenius norm.

In our numerical test, we solve the least squares problem (29) for increasing values of k and plot on a logarithmic scale the norm of the vector  $\beta^k = (\beta_1, \dots, \beta_k)$  versus the norm of the residual of the equation (29). In a separate panel, we also plot the relative error in the

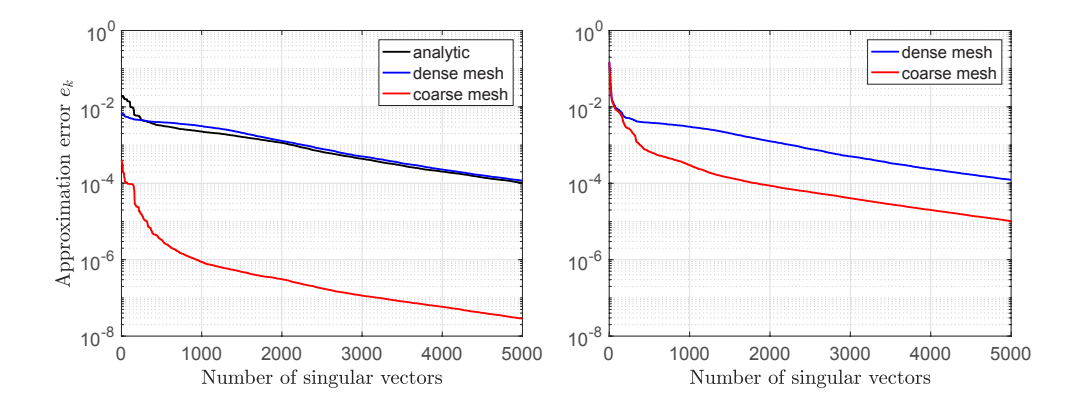


**Figure 6.** The discrepancy between the matrix  $X_{\sigma}$  and its projection onto the affine subspace corresponding to the feature matrices extracted from the non-centered sample,  $Q_k = \text{span}\{U_1, \dots, U_k\}$ , measured in the relative Frobenius norm (37). The left panel corresponds to the constant conductivity, and the right one to the smooth conductivity of figure 1. The different curves correspond to how the Dirichlet-to-Neumann matrix was approximated. The coarse mesh is that used to generate the sample, leading to lowest error. The dense mesh is that used to generate the resistance data, and is denser than the mesh used to generate the sample.

estimated Dirichlet-to-Neumann matrix (38) comparing it to the matrix computed with the fine FEM mesh:

$$\mathscr{E}_k = \frac{\|\widehat{\mathsf{L}}_\sigma^{n,k} - \mathsf{L}_\sigma^n\|_F}{\|\mathsf{L}_\sigma^n\|_F}.$$

To further our understanding, we investigate which of the spectral components of the matrix are estimated most reliably by defining the truncation operator

$$\mathscr{T}_p: \mathbb{R}^{(n+1)\times (n+1)} \to \mathbb{R}^{(2p+1)\times (2p+1)}, \quad [A_{ij}]_{0\leqslant i,j\leqslant n} \mapsto [A_{ij}]_{0\leqslant i,j\leqslant p},$$

where  $p \le n/2$ , i.e.  $\mathcal{T}_p(A)$  is the  $(2p+1) \times (2p+1)$  upper left block of the original matrix, and the restricted error is defined as

$$\mathscr{E}_k^p = \frac{\|\mathscr{T}_p(\widehat{\mathsf{L}}_\sigma^{n,k} - \mathsf{L}_\sigma^n)\|_F}{\|\mathscr{T}_p(\mathsf{L}_\sigma^n)\|_F}.$$
(39)

The index *p* indicates the spectral band in which the reconstruction is assessed. We run the test both with no artificial noise added to data, the error being the model discrepancy, and a low level Gaussian uncorrelated noise with standard deviation 0.1% of the maximum entry of the conductance matrix is added to it. As pointed out earlier, we cannot expect good performance for reconstructing high frequency components of the Dirichlet-to-Neumann map based on the low frequency electrode data.

Figure 7 shows the results when the data comes from a smooth conductivity distribution. The relative error displays the characteristic semiconvergence property, decreasing at first, then increasing when the addition of new feature vectors starts to deteriorate the results. As expected, the relative reconstruction error is smaller in the lower spectral band, in agreement with the understanding that the 16-electrode resistance data cannot contain much information outside the low frequency band. Interestingly, the semiconvergence behavior for few feature vectors is similar whether artificial noise is added or not, the difference being mostly

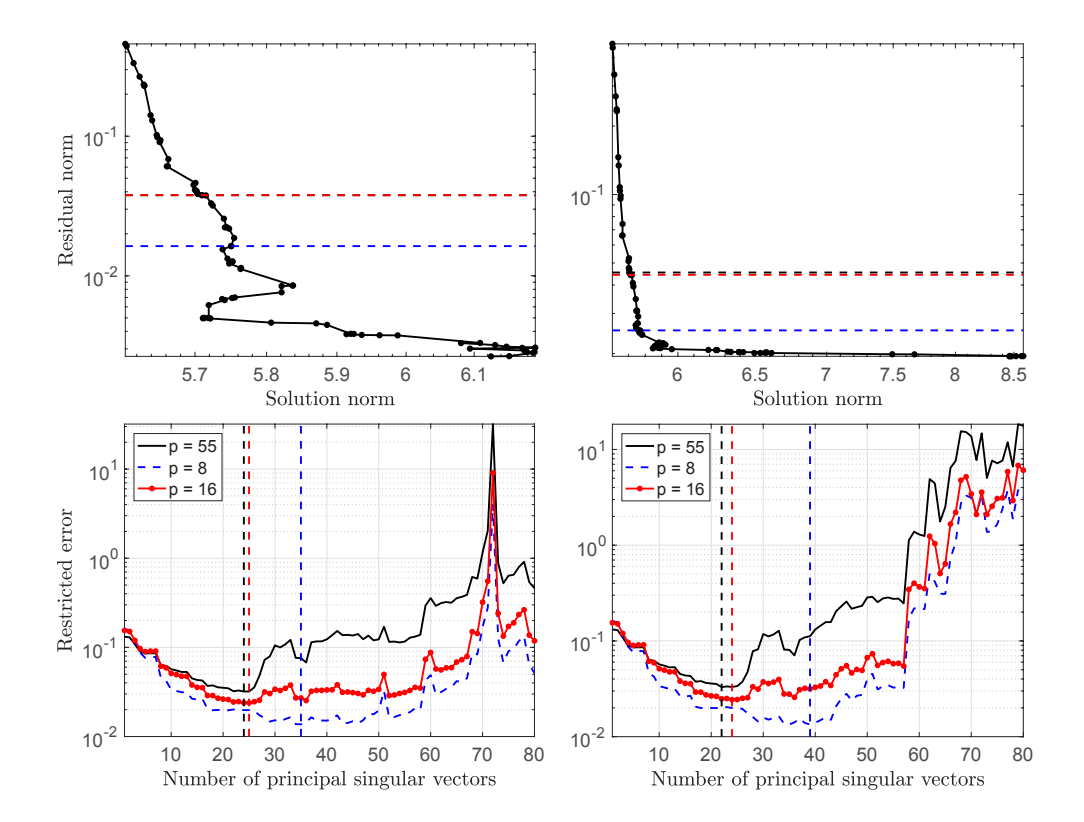


**Figure 7.** Results corresponding to the smooth conductivity distribution. Left column, top: The L-curve, displaying the norm of the solution (horizontal axis) versus the norm of the residual (vertical axis), both in logarithmic scale. The curve is parametrized by the number of PCA feature vectors included in the model No artificial noise is added to the numerically computed conductance matrix used as data. Bottom: The semiconvergence behavior of the relative error in the Dirichlet-to-Neumann matrix, the different curves corresponding to different numbers of Fourier components included in the analysis, as indicated by the legend. The horizontal dashed lines indicate the number of PCA basis vectors that correspond to the minimum. The numbers yielding the minimum are indicated in the top figure by horizontal lines. Observe that the black and the red horizontal lines are indistinguishable. Right column: The same computations with Gaussian uncorrelated noise of standard deviation 0.1% of the maximum entry of the conductance matrix is added to the conductance matrix entries.

marked for larger values of k where the estimate is highly unreliable anyway. Unfortunately, the L-curve cannot be used as a reliable stopping criterion, because the residual continues to decrease without the norm of the solution increasing significantly way after the minimum relative error is reached.

We ran the same test with data coming from a discontinuous conductivity distribution. While the prior distribution that was used to generate the sample is not representative for this conductivity, the ill-posedness of the EIT inverse problem suggests that the performance should be similar to the smooth conductivity. The results shown in figure 8 are qualitatively very similar to the ones with the smooth conductivity, confirming the intuition that since the Dirichlet-to-Neumann map is not sensitive to fine details in the conductivity such as smoothness, as the ill-posedness of the EIT problem suggests, only the large scale features matter.

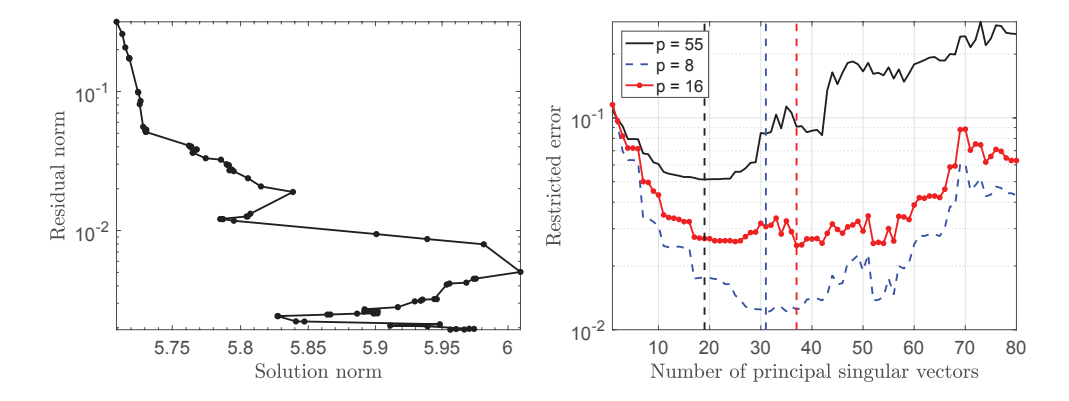


**Figure 8.** The results as in figure 7, with the difference that the data arise from an underlying non-smooth conductivity shown in figure 1 (right) for which the random conductivity model used for the generation of the PCA basis is not representative. Here, no artificial noise to the data was added.

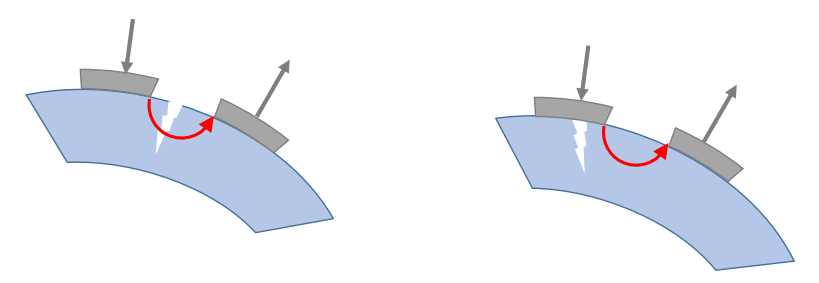


**Figure 9.** Two cartoons illustrating the effect of electrode positions on sensitivity. On the left, a high frequency detail of the conductivity, such as a crack, is located between two adjacent electrodes, causing a significant effect on the voltage difference maintaining a prescribed current flow between the electrodes, while on the right, the crack is under a contact electrode, having little effect on the voltage difference.

#### 7. Discussion

This article discusses the analytical and numerical relation of the idealized boundary data of the EIT problem formulated in terms of the Dirichlet-to-Neumann map and the realistic resistance map corresponding to the real measurement protocol using contact electrodes. It is shown that the problem of estimating the former from the latter can itself be recast as an illposed inverse problem. The analysis provides a formula for computing of the resistance map from the matrix approximation of the Dirichlet-to-Neumann map. The difficulties in approximating the latter from electrode measurements are manifold. First, in order to not introduce significant modeling errors in the matrix equation by truncation, it is necessary to include high frequencies. However, the electrode data may have only limited sensitivity to high frequencies of the conductivity, further affecting the high frequency components of the Dirichlet-to-Neumann map, and moreover, the sensitivity to high frequency details may depend on the position of the electrodes. To understand the latter statement, consider a conductivity with a high frequency detail such as a crack near the boundary, as illustrated by the two cartoons in figure 9. Assuming that the crack is modeled as a sharp decrease in conductivity, if a singularity is located between two electrodes, as in the cartoon on the left, in order to maintain the current between the adjacent electrodes, a significant increase in voltage difference is observed. However, if the same singularity is under an electrode, as in the cartoon on the right, since the current density is strongly concentrated at the edges of the electrodes [28] the effect on voltages is less pronounced. In this article, the high frequency effects due to the boundary behavior of the conductivity are to some extent mitigated by assuming *a priori* that the conductivities are smooth and have low variance near the boundary. Nevertheless, as shown by numerical examples, selection of the truncation level in the computations is not a simple issue. To decide how much details in the Dirichlet-to-Neumann map are estimated from the resistance map, we used the PCA basis, where the idea is to let the simulated data to decide the level of details included. The numerical experiments demonstrate that the resistance map does not allow reliable reconstruction of the high frequency Fourier modes of the Dirichlet-to-Neumann map: if L is the number of the electrodes, one cannot hope to recover effectively much more than L/2 sine and cosine coefficients, in line with the classical Nyquist sampling limit. Finally, as shown by the numerical experiments, the results depend on the finite element discretization level.

The numerical tests in this article were performed with a low resolution 16 electrode model. A future work includes the increase of the resolution by adding more electrodes, and using a higher order FEM computations to better take into account the voltage singularities at the electrode boundaries, thus diminishing the modeling error that even in the absence of additive noise is enough to produce significant reconstruction error in the Dirichlet-to-Neumann map. The principal component approach suggested in this paper, while computationally convenient as it linearizes the inverse problem, may not be the optimal, as it does not use analytical properties of the Dirichlet-to-Neumann map that could be implemented as a prior. Another important question requiring further investigation is to find a robust and reliable criterion for choosing the number of PCA components, corresponding to choosing the regularization level. As pointed out, the analog of an L-curve method does not work here, possibly because a significant part of the noise is strongly correlated modeling error. The viability of the suggested method as an initial preprocessing step for the EIT problem should be tested in connection with an EIT inverse solver based on the Dirichlet-to-Neumann map, such as the d-bar method or layer stripping. However, the quality of the results depends on the selection of the particular reconstruction method as well as on its implementation. This question will be addressed in later work.

#### **Acknowledgments**

The work of DC was partly supported by NSF grant DMS-1522334, and of SN and ES by NSF grant DMS-1714617.

#### **ORCID iDs**

D Calvetti https://orcid.org/0000-0001-5696-718X E Somersalo https://orcid.org/0000-0001-5099-3512

#### References

- [1] Barber D C and Brown B H 1984 Applied potential tomography J. Phys. E: Sci. Instrum. 17 723–33
- [2] Calderón A P 1980 On an inverse boundary value problem *Seminar on Numerical Analysis and its Applications to Continuum Physics* (Rio de Janerio: Soc Brasileira de Matematica)

- [3] Calvetti D, Dunlop M, Somersalo E and Stuart A 2017 Iterative updating of model error for Bayesian inversion *Inverse Problems* 34 025008
- [4] Calvetti D, Ernst O and Somersalo E 2014 Dynamic updating of numerical model discrepancy using sequential sampling *Inverse Problems* 30 114019
- [5] Calvetti D, Hadwin P J, Huttunen J M J, Isaacson D, Kaipio J P, McGivney D, Somersalo E and Volzer J 2015 Artificial boundary condition and domain truncation in electrical impedance tomography. Part I: theory and preliminary examples *Inverse Problems Imaging* 9 749–66
- [6] Calvetti D, Hadwin P J, Huttunen J M J, Isaacson D, Kaipio J P and Somersalo E 2015 Artificial boundary condition and domain truncation in electrical impedance tomography. Part II: computed examples *Inverse Problems Imaging* 9 767–89
- [7] Cheney M, Isaacson D and Newell J C 1999 Electrical impedance tomography SIAM Rev. 41 85–101
- [8] Cheng K-S, Isaacson D, Newell J C and Gisser D G 1989 Electrode models for electric current computed tomography IEEE Trans. Biomed. Eng. 3 918–24
- [9] Evans L C 2010 *Partial Differential Equations* 2nd edn (Providence, RI: American Mathematical Society)
- [10] Garde H and Staboulis S 2017 Convergence and regularization for monotonicity-based shape reconstruction in electrical impedance tomography *Numer. Math.* 135 1221–51
- [11] Grisvard P 2011 Elliptic Problems in Nonsmooth Domains vol 69 (Philadelphia, PA: SIAM)
- [12] Hanke M, Harrach B and Hyvönen N 2011 Justification of point electrode models in electrical impedance tomography Math. Mod. Methods Appl. Sci. 21 1395–413
- [13] Hyvönen N 2009 Approximating idealized boundary data of electric impedance tomography by electrode measurements Math. Mod. Methods Appl. Sci. 19 1185–202
- [14] Hyvönen N 2009 Comparison of idealized and electrode Dirichlet-to-Neumann maps in electric impedance tomography with an application to boundary determination of conductivity *Inverse Problems* 25 085008
- [15] Ikehata M and Siltanen S 2000 Numerical method for finding the convex hull of an inclusion in conductivity from boundary measurements *Inverse Problems* 16 1043–52
- [16] Isaacson D, Mueller J L, Newell J C and Siltanen S 2004 Reconstructions of chest phantoms by the D-bar method for electrical impedance tomography *IEEE Trans. Med. Imaging* 23 821–8
- [17] Järvenää S and Somersalo E 1996 Impedance imaging and electrode models *Inverse Problems and Medical Imaging and Nondestructive Testing* ed H W Engl *et al* (New York: Springer)
- [18] Joliffe I T 2002 Principal Component Analysis (New York: Springer)
- [19] Kirsch A 2005The factorization method for a class of inverse elliptic problems *Math. Nachr.* **278** 258–77
- [20] Knudsen K, Lassas M, Mueller J and Siltanen S 2009 Regularized D-bar method for the inverse conductivity problem *Inverse Problems Imaging* 3 599–624
- [21] Nachman A I 1996 Global uniqueness for a two-dimensional inverse boundary value problem Ann. Math. 143 71–96
- [22] Nazarov A I and Repin S I 2015 Exact constants in Poincaré type inequalities for functions with zero mean boundary traces *Math. Methods Appl. Sci.* **38** 3195–207
- [23] Persson P O and Strang G 2004 A simple mesh generator in MATLAB SIAM Rev. 46 329–45
- [24] Roininen L, Lehtinen M S, Lasanen S, Orispää M and Markkanen M 2011 Correlation priors Inverse Problems Imaging 5 167–84
- [25] Roininen L, Huttunen J M and Lasanen S 2014 Whittle-Matérn priors for Bayesian statistical inversion with applications in electrical impedance tomography *Inverse Problems Imaging* 8 561-86
- [26] Siltanen S, Mueller J and Isaacson D 2000 An implementation of the reconstruction algorithm of a Nachman for the 2D inverse conductivity problem *Inverse Problems* 16 681
- [27] Somersalo E, Cheney M, Isaacson D and Isaacson E 1991 Layer stripping: a direct numerical method for impedance imaging *Inverse Problems* 7 899
- [28] Somersalo E, Cheney M and Isaacson D 1992 Existence and uniqueness for electrode models for electric current computed tomography SIAM J. Appl. Math. 52 1023–40
- [29] Sylvester J and Uhlmann G 1987 A global uniqueness theorem for an inverse boundary value problem Ann. Math. 125 153–69
- [30] Tamburrino A and Rubinacci G 2002 A new non-iterative inversion method for electrical resistance tomography *Inverse Problems* 18 1809–29

- [31] Vauhkonen M, Vadasz D, Karjalainen PA, Somersalo E and Kaipio J P 1998 Tikhonov regularization and prior information in electrical impedance tomography IEEE Trans. Med. Imaging 17 285–93
- [32] Vauhkonen M, Lionheart W R, Heikkinen L M, Vauhkonen P J and Kaipio J P 2001 A MATLAB package for the EIDORS project to reconstruct two-dimensional EIT images *Physiol. Meas.* 22 107
- [33] Vauhkonen P J, Vauhkonen M, Savolainen T and Kaipio J P 1999 Three-dimensional electrical impedance tomography based on the complete electrode model *IEEE Trans. Biomed. Eng.* 46 1150–60